ROYAL SOCIETY
OF CHEMISTRY

PAPER

Check for updates

Electronic structure, absorption spectra and oxidation dynamics in polyynes and dicyanopolyynes†

Lazaros Chalkopiadis, [ID] Konstantinos Lambropoulos [ID] and Constantinos Simserides [ID] *

The advent of femtosecond to attosecond experimental tools has made now possible to study such ultrafast carrier dynamics, *e.g.*, the spatial and temporal charge density evolution, after an initial oxidation or reduction in molecules, candidates for atomic wires like polyynes and dicyanopolyynes. Here, we study the electronic structure and hole transfer in symmetric molecules containing carbon, nitrogen and hydrogen, the first members in the series of polyynic carbynes and dicyanopolyynes, using methods based on density functional theory (DFT): constrained DFT (CDFT), time-dependent DFT (TDDFT) and real-time TDDFT (RT-TDDFT), with Löwdin population analysis, comparing many levels of theory and obtaining convergence of the results. For the same purposes, we develop a tight binding (TB) variant using all valence orbitals of all atoms. This TB variant is applied here in linear molecules, but it is also adequate for electronic structure, charge transfer and charge transport of non-linear molecules and clusters of molecules. We calculate the electronic structure, the time-dependent dipole moment and the probabilities of finding the hole at each site, their mean over time values, the mean transfer rates from the oxidation site to other sites and the frequency content (using charge as well as dipole moment oscillations). We take into account zero-point motion. The initial conditions for RT-TDDFT are obtained by CDFT. For TB, we explore different initial conditions: we place the hole at a particular orbital or distribute it among a number of orbitals; it is also possible to include phase differences between orbitals. Finally, we compare with available experimental data.

1 Introduction

The 2023 Nobel Prize in Physics[1] was awarded to P. Agostini, F. Krausz and A. L'Huillier "for experimental methods that generate attosecond pulses of light for the study of electron dynamics in matter": overtones were utilized[2,3] and pulses of the order of 0.25[4] to 0.65[5] femtoseconds were created. This achievement enabled the investigation of extremely rapid processes that were previously impossible to follow. Such light pulses are short enough to enable the study of electrons moving in atoms, molecules, and condensed matter. Attosecond pulses can be produced, observed, measured and used as a new experimental tool: attosecond spectroscopy. It is now possible to produce pulses of the order of tenths of femtoseconds.

The application of isolated attosecond pulses to prompt ionization of phenylalanine and the subsequent detection of

ultrafast dynamics on a sub-4.5 femtosecond scale, shorter than the vibrational response of the molecule, showed that it is possible to follow carrier dynamics in polyatomic molecules: attosecond science is progressively moving towards investigation of more complex systems.[6] A UV laser of λ = 300 nm corresponds to a period of 1 fs, while, a XUV photon of λ = 30 nm corresponds to a period of 0.1 fs. It is therefore possible, employing high harmonic generation (HHG), to break the 1 fs limit. In HHG, usually, a sample like gas, plasma, *etc.* is illuminated by a laser's pulses, and emits high harmonics of the generation beam (above 5th harmonic). Hence, in this coherent process, HHG can be used to obtain attosecond pulses. A recent discussion on open questions in attochemistry and a comparison with femtochemistry[7] is given in ref. 8. Oxidation dynamics can be studied today in a variety of molecules and is experimentally relevant. For example, charge transfer has been recently studied in cyclo[18]carbon,[9] DNA dimers[10] and in *para*-functionalized bromobenzene molecules.[11] This work is devoted to such extremely fast hole dynamics, *i.e.*, to the spatial and temporal charge density evolution, after an initial oxidation, in molecules candidates for atomic wires: polyynes and dicyanopolyynes.

Department of Physics, National and Kapodistrian University of Athens, Panepistimiopolis, Zografos GR-15784, Athens, Greece.
E-mail: csimseri@phys.uoa.gr

This journal is © the Owner Societies 2024

Phys. Chem. Chem. Phys., 2024, **26**, 22149–22163 | **22149**

In 2010 a polyynic chain of 44 atoms was synthesized.[12] Later, it became possible to establish a route for the mass production of long and stable chains composed of more than 6000 carbon atoms inside double-walled carbon nanotubes.[13] Electrical transport measurements of carbon atom chains were performed in 2013.[14] Thermal,[15–18] vibrational,[19–21] mechanical[16,22] and electrical transport[14,23–27] properties were studied, too. Structure-modulated charge transfer in carbon atomic wires was claimed in chains with different end groups.[28] Based on the experience from DNA charge transfer experiments, it appears that a possible technique for achieving reliable charge transfer measurements is time-resolved spectroscopy;[29–35] usually a pulsed laser is used to excite (pump) and measure the absorption (probe) of a sample as a function of time. Temporal resolution in the femtosecond to attosecond regime should be achieved for reliable measurements in atomic wires, as theory predicts phenomena of the order of femtoseconds.[9,36]

We notice the large persistence length of one-dimensional carbon chains. In 2013, the persistence length, ℓ_p, of carbynes at 300 K was roughly estimated at 14 nm or about 110 carbon atoms in a row;[37] this is large compared to persistence lengths of important polymers. In 2016 long and stable polyyinc chains composed of more than 6000 carbon atoms inside double-walled carbon nanotubes were produced.[13] This would mean a persistence length of roughly 1000 nm = 1 μm. Even without this development,[13] carbyne is relatively stiff for a polymer, comparable to graphene nanoribbons, 1/3 times as stiff as a double-stranded DNA (dsDNA) rod (it should be taken into account that dsDNA has a diameter of 2 nm, i.e., it is not atom-thick as carbon chains are). In 2024 it was announced[38] that stable interlocked polyynes bearing several macrocycles were prepared, including a [5]rotaxane having 34 contiguous alkynes with properties similar to those of carbyne.

We are also interested in dicyanopolyynes, consisting of an unsaturated linear skeleton of carbon atoms ended by a cyano group at each edge, i.e., $N\equiv C-(C\equiv C-)_m C\equiv N$ ($m = 0, 1, \ldots$). The formation of these rod-shaped molecules in carbon plasma, was reported in 1993;[39] they form a homologous series of nitrogen-end-capped linear sp carbon chains.[40] A theoretical study of the structure and properties of polyynes, monocyano- and dicyanopolyynes was published later,[41] followed by semi-empirical calculation of their electronic absorption wavelengths, and predictions regarding long-chain compounds, including an estimation of the absorption wavelength (ca. 400 nm or ca. 3.0 eV) of the hypothetical (infinite) carbon allotrope carbyne.[42] The various flavours of energy gap[43] could reveal underlying physics, e.g., excitonic effects. Using DFT,[36,44] a gap of 0.8 eV was obtained for long chains; this coincides with that obtained by a simple TB wire model with a parametrization extracted via DFT at the same level of theory as explained by the method introduced in ref. 45. The same TB wire model with the empirical Harrison expressions[46,47] gives a gap of 0.32 eV. A large range of energy gaps can be found in the literature,[24,48,49] depending on the calculation method. Generally, DFT with exchange–correlation functionals that do not include exact exchange tends to significantly underestimate the energy gap; higher level theories, and the employment of hybrid
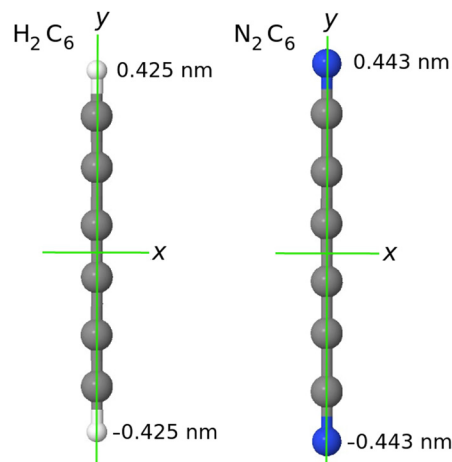

Fig. 1 In our system of coordinates the y axis is identified with the D_∞ axis. As example: a comparison of the H_2C_6 versus the N_2C_6 geometry.

functionals in DFT with adequate percentage of exact exchange can deal with the problem,[50] as larger percentages of exact exchange lead to broadening of the energy gap.

In 2004 a mixture of dicyanopolyynes was formed and collected when graphite electrodes were arced in liquid nitrogen.[51] Dicyanopolyynes have been recently detected in space. The detection of dicyanopolyynes is hampered by their nonpolar nature; they cannot be observed through their rotational spectra. The presence of NCCN in interstellar and circumstellar clouds can be inferred through observation of chemically related polar molecules, such as protonated cyanogen (NCCNH$^+$)* or the metastable isomer isocyanogen CNCN.[52] NCCN and NCCCCN formation in Titan's atmosphere has been suggested.[52] Recently, in 2015, protonated cyanogen (NCCNH$^+$)* was detected in the cold dark clouds L483 and TMC-1.[53] From the observed abundances of NCCNH$^+$, it was inferred that indeed cyanogen (NCCN) should be as abundant as the nitriles HCN and HC$_3$N. In 2018, isocyanogen (CNCN) was discoverd in interstellar space, giving further evidence that dicyanopolyynes are abundant in space.[54] Finally, in 2023, interstellar NC4NH$^+$ was discovered, adding to the bulk of evidence regarding the presence and quantity of dicyanopolyynes in space.[55]

Carbynes or atomic carbon chains are conceptually divided into cumulenic (equidistant carbon atoms) and polyyinc (alternating longer and shorter bonds between consecutive carbon atoms). We will only consider here polyyinc chains with even carbon atoms, starting with a short bond between carbons; this results in purely rod-like molecules, cf. Fig. 1. Dicyanopolyynes are also rod-like. In this work, we study hole transfer‡, the temporal and spatial evolution of a hole after its creation, i.e., oxidation dynamics, in the first members in the series of linear

---

‡ *Charge transfer* refers to intramolecular or intermolecular motion of electrical carriers in the absence of an external driving force (e.g. voltage, temperature gradient). After oxidation or reduction, a hole or an extra electron, respectively, are initially created or injected at a site of a molecular system; subsequently, the carrier spontaneously moves to other energetically more favorable sites. *Charge transport* implies application of an external driving force.

22150 | *Phys. Chem. Chem. Phys.*, 2024, **26**, 22149–22163

This journal is © the Owner Societies 2024

polyynic carbynes and dicyanopolyynes, which can be useful as molecular wires. We compare alternative theoretical approaches, based on tight binding (TB) using all valence orbitals, and density functional theory (DFT), both for the time-independent and the time-dependent problem. Recently, we have studied hole oscillations within the C18 carbon ring, including zero-point vibrations with a Monte Carlo (MC) sampling technique, comparing with the static cumulenic and polyynic equilibrium configurations.[9] Here, we extend this study to polyynes and dicyanopolyynes.

Let us call N_C, N_N, and N_H the total number of carbon, nitrogen, and hydrogen atoms in a molecule. In finite carbynes, the end groups can be methine (CH–) or methylene (CH$_2$–) or methyl (CH$_3$–) as explained below. Cumulenes with even (odd) N_C have D_{2h} (D_{2d}) symmetry with their methylene (CH$_2$–) groups being coplanar (perpendicular) to each other. Polyynes with odd N_C have C_{3v} symmetry; one end group being methine (CH–), the other methyl (CH$_3$–). Polyynes with even N_C and two CH$_3$– end groups can be found in eclipsed (D_{3h}) and staggered (D_{3d}) symmetry. Finally, polyyynes with even N_C and two CH– end groups have $D_{\infty h}$ symmetry. Dicyanopolyynes have always N_N = 2, the nitrogen atoms being at the ends of the molecule and possess $D_{\infty h}$ symmetry.

This article is organized as follows. In Section 2 we display our theoretical arsenal, concerning TB-related techniques (Subsection 2.1) or DFT-related techniques (Subsection 2.2). In Section 3 we present and discuss our results for polyynes (Subsection 3.1) and dicyanopolyynes (Subsection 3.2). In Section 4 we arrive at conclusions. Finally, we include online ESI.†

2 Theory

2.1 Tight binding (TB)

We describe below a TB approach for the calculation of electronic band structure (time-independent problem) and for carrier evolution (time-dependent problem), where the molecular states are written as combination of atomic valence states of all atoms.

2.1.1 Time-independent problem. We consider the state $|\Psi\rangle$ of a molecule as a linear combination of all valence atomic states $|\phi_{n,i}\rangle$: 2s, 2p$_x$, 2p$_y$, 2p$_z$ for C and N atoms and 1s for H atoms, i.e.,

$$|\Psi\rangle = \sum_{n=1}^{N} \sum_{i=1}^{I} c_{ni}|\phi_{ni}\rangle, \tag{1}$$

where n is the atom index and i the atomic valence state index. This analysis of the molecular state into valence atomic state components, constitutes the character of the molecular state, e.g., if the constituting components are mainly 2p states and overlap laterally, the character is π. $|\Psi\rangle$ obeys the Schrödinger equation

$$\hat{H}|\Psi\rangle = E|\Psi\rangle, \tag{2}$$

where $\hat{H}$ is the molecular Hamiltonian. Defining

$$S_{mjni} := \langle\phi_{mj}|\phi_{ni}\rangle = \delta_{nm}\delta_{ij}, \tag{3}$$

$$H_{mjni} := \langle\phi_{mj}|\hat{H}|\phi_{ni}\rangle, \tag{4}$$

we obtain

$$\sum_{n=1}^{N} \sum_{i=1}^{I} \left(H_{mjni} - E\delta_{nm}\delta_{ij}\right)c_{ni} = 0, \tag{5}$$

or alternatively written,

$$H\vec{v} = E\vec{v}, \tag{6}$$

$$\vec{v} = \begin{bmatrix} c_{11} \\ \vdots \\ c_{ni} \\ \vdots \\ c_{NI} \end{bmatrix}. \tag{7}$$

The solution of the system (5) is given by numerical diagonalisation. For this purpose, we need the Hamiltonian matrix elements H_{mjni}. For the diagonal matrix elements H_{nini}, also known as on-site energies, we use the parametrization $E_H(1s) = -13.64$ eV, $E_C(2s) = -13.54$ eV, $E_C(2p_x) = -7.47$ eV, $E_C(2p_y) = -7.85$ eV, $E_C(2p_z) = -7.47$ eV, $E_N(2s) = -16.49$ eV, $E_N(2p_x) = -12.84$ eV, $E_N(2p_y) = -8.34$ eV, $E_N(2p_z) = -12.84$ eV. For the non-diagonal matrix elements H_{mjni} ($m \neq n$), referring to nearest neighboring atoms, we utilize the Slater–Koster two-center interaction transfer integrals[56]

$$V_{ss} = V_{ss\sigma}, \tag{8}$$

$$V_{sx} = \xi_1 V_{sp\sigma}, \tag{9}$$

$$V_{xx} = \xi_1^2 V_{pp\sigma} + \left(1 - \xi_1^2\right)V_{pp\pi}, \tag{10}$$

$$V_{xy} = \xi_1\xi_2(V_{pp\sigma} - V_{pp\pi}), \tag{11}$$

where ξ_1 and ξ_2 are directional cosines of $\vec{d} = \vec{ij}$, which point from atom i to atom j, s stands for s-type orbitals and x, y, z stand for the corresponding p-type orbitals. For other cases a circular permutation of indexes is implied. For the values of $V_{ss\sigma}$, $V_{sp\sigma}$, $V_{pp\sigma}$, $V_{pp\pi}$, we use the Harrisson[46,47] expressions

$$V_\chi = \chi\frac{\hbar^2}{m_e d^2}, \tag{12}$$

where m_e is the electron mass and d the two-center distance. In our parametrization, we use the χ values: $\chi_{ss\sigma} = -1.23$, $\chi_{sp\sigma} = -1.42$, $\chi_{pp\sigma} = 2.29$, $\chi_{pp\pi} = -0.78$, slightly modified relative to the original Harrison constants. For interactions involving the H 1s atomic orbital, the expression is multiplied by a factor $b = 0.65$ for each H 1s orbital involved. For non-diagonal matrix elements of non nearest neighboring atoms, we assume $H_{mjni} = 0$ ($m \neq n$). Our parametrization was obtained by fitting our TB numerical results with the experimental excitation and ionization energies of our polyynes and dicyanopolyynes, cf. Fig. 5 and 11. We used the Nelder–Mead multidimensional simplex method. We notice that HOMOs and LUMOs are usually (cf. ESI†) of π-like symmetry, involving 2p$_x$ and 2p$_z$ orbitals of C and N, i.e., those perpendicular to the molecular axis, y. Hence, our parametrization is mainly tested against 2p$_x$ and 2p$_z$ on-site

This journal is © the Owner Societies 2024

Phys. Chem. Chem. Phys., 2024, **26**, 22149–22163 | **22151**

energies of C and N and there is less fidelity about the values obtained for 2s and $2p_y$ on-site energies of C and N. With this parametrization we achieve: in polyynes, RMSE 0.16 eV for the ionization energy and 0.19 eV for the excitation energy and in dicyanopolyynes RMSE 0.27 eV for the ionization energy.

2.1.2 Time-dependent problem. The time-dependent problem is the evolution of the molecular state in time, after having defined an initial condition. We have to solve the time-dependent Schrödinger equation

$$i\hbar\frac{\partial}{\partial t}|\Psi(t)\rangle = \hat{H}|\Psi(t)\rangle. \tag{13}$$

$|\Psi(t)\rangle$ is written as linear combination of $|\phi_{ni}\rangle$ with time-dependent coefficients, i.e.,

$$|\Psi(t)\rangle = \sum_{n=1}^{N}\sum_{i=1}^{I} C_{ni}(t)|\phi_{ni}\rangle. \tag{14}$$

Combining eqn (13) and (14), we obtain

$$i\hbar\dot{C}_{mj}(t) = \sum_{n=1}^{N}\sum_{i=1}^{I} C_{ni}(t)H_{mjni}. \tag{15}$$

Eqn (15) in matrix form is

$$\dot{\vec{X}}(t) = -\frac{i}{\hbar}H\vec{X}(t), \tag{16}$$

where H is the Hamiltonian matrix and $\vec{X}(t)$ is

$$\vec{X}(t) = \begin{bmatrix} C_{11}(t) \\ \vdots \\ C_{ni}(t) \\ \vdots \\ C_{NI}(t) \end{bmatrix}. \tag{17}$$

Alternatively, we can use the collective index $k = 1, 2,\ldots,K$ standing for indexes n and i, i.e., $k := \{ni\}$. We look for a solution of the differential eqn (16) of the form

$$\vec{X}(t) = \vec{v}e^{-\frac{i}{\hbar}Et}. \tag{18}$$

Using eqn (16)–(18), we obtain

$$H\vec{v} = E\vec{v}, \tag{19}$$

i.e., the eigenvalue-eigenvector problem of eqn (6). After obtaining the eigenvalues E_k and eigenvectors $\vec{v}_k$, if the eigenvectors are linearly independent, the general solution is

$$\vec{X}(t) = \sum_{k=1}^{K} \sigma_k \vec{v}_k e^{-\frac{i}{\hbar}E_k t}, \tag{20}$$

where σ_k are determined by the initial conditions.

A trivial initial condition would be to make the oxidation (create the hole) at a specific atomic orbital ℓ; then we have to set the corresponding coefficient $\sigma_\ell = 1$ and the remaining coefficients $\sigma_{k\neq\ell} = 0$. If we need to create the carrier not at a specific atomic orbital but at a specific atom, many atomic

orbitals are involved. Various choices can be made in such a case. We can even use different phases for the orbitals of the same atom. In the following example, for the first atom (e.g. a Carbon), we set a phase difference $\frac{\pi}{2}$ between the 2s, $2p_x$, $2p_y$ orbitals, simultaneously imposing identical occupation of all second shell orbitals (including $2p_z$). However, in the results shown in this article, we set the phase difference zero. This initial condition is denoted by (1,1,1,1).

$$\vec{X}(0) = \begin{bmatrix} C_{11}(0) \\ C_{12}(0) \\ C_{13}(0) \\ C_{14}(0) \\ \vdots \\ C_{ni}(0) \\ \vdots \\ C_{NI}(0) \end{bmatrix} = \begin{bmatrix} \frac{1}{2}e^{i\frac{\pi}{2}} \\ \frac{1}{2} \\ \frac{1}{2}e^{-i\frac{\pi}{2}} \\ \frac{1}{2} \\ \vdots \\ 0 \\ \vdots \\ 0 \end{bmatrix}. \tag{21}$$

Similarly, we denote initial conditions for (2s, $2p_x$, $2p_y$, $2p_z$) by setting the respective symbol to one, at the position where the carrier is placed. For example, (1,1,1,0) means initial condition $\left(\frac{1}{\sqrt{3}}e^{i\frac{\pi}{2}}, \frac{1}{\sqrt{3}}, \frac{1}{\sqrt{3}}e^{-i\frac{\pi}{2}}, 0\right)$, if a phase difference $\frac{\pi}{2}$ is imposed. However, in the results shown in this article, we set the phase difference zero. Obviously, there is an infinite number of initial conditions that one could imagine. A comparison of the H_2C_6 versus the N_2C_6 geometry is given in Fig. 1 in a system of coordinates, where the y axis is identified with the D_∞ axis. Then, the (1,1,1,1) initial condition treats $2p_x$ and $2p_z$ in exactly the same way.

The TB variant that we use requires one s-type orbital for hydrogen, as well as one s-type orbital and a triplet of p-type orbitals for carbon or nitrogen. This is similar to the idea behind the "minimal" STO-nG basis set, since it has the same number and type (although Gaussian) of valence orbitals. The "TB STO-3G" initial condition that will be used below means that we take the initial carrier percentages from CDFT with the STO-3G basis set and use the same numbers for the TB initial condition.

2.2 DFT, CDFT, TDDFT, RT-TDDFT, geometry optimization, vibrational modes

DFT[57,58] is a well-established, widely-used method for the study of ground state properties of many-body systems like molecules and solids. The ground state is determined by self-consistently solving the Kohn–Sham equations that represent a system of N non-interacting electrons, assumed to produce the same charge density as the real system of N interacting electrons. Later DFT

22152 | Phys. Chem. Chem. Phys., 2024, **26**, 22149–22163

This journal is © the Owner Societies 2024

was extended[59] to time dependent systems. Today, time-dependent DFT (TDDFT) is usually applied to study excited states. The time-dependent Kohn–Sham (TDKS) equations with an effective potential energy $v_{KS}(\vec{r},t)$, in atomic units (a.u.), read

$$i\frac{\partial}{\partial t}\Psi_j(\vec{r},t) = \left[-\frac{1}{2}\nabla^2 + v_{KS}(\vec{r},t)\right]\Psi_j(\vec{r},t), \quad j = 1, ..., N \quad (22)$$

where $\{\Psi_j(\vec{r},t)\}$ is a set of fictitious orbitals, and

$$v_{KS}(\vec{r},t) = v_{ext}(\vec{r},t) + v_H(\vec{r},t) + v_{xc}[\rho](\vec{r},t) \quad (23)$$

$v_{ext}(\vec{r},t)$ includes external fields and nuclear potentials, $v_H(\vec{r},t)$ is the Hartree potential, and $v_{xc}[\rho](\vec{r},t)$ are the exchange and correlation terms. The total time-dependent charge density is

$$\rho(\vec{r}, t) = \sum_{j=1}^{N_{occ}} \left|\Psi_j(\vec{r},t)\right|^2, \quad (24)$$

i.e., it is the sum of the charge density of all occupied orbitals $j = 1, 2, \ldots, N_{occ}$. Within TDDFT, the above system of equations is solved using the linear response method, which is not actually a time-resolved method: the TDKS equations are solved in the frequency domain to obtain the excitation energies of a system subject to a small perturbation. Later, real-time TDDFT (RT-TDDFT) was established. RT-TDDFT[60] is based on a direct numerical integration of the above TDKS equations. The TDKS equations are solved and the electron density is obtained at each time step. The density is then used to calculate the Hamiltonian in the next cycle of the self-consistent process. Our DFT, TDDFT, and RT-TDDFT calculations were performed using NWChem.[61]

For RT-TDDFT simulations, we initially perform a ground-state DFT calculation on the neutral molecule and obtain the charge at each atom *via* Löwdin population analysis.[62] For the calculation of absorption spectra, we obtain the time-dependent dipole moment in each of the *x*, *y* and *z* axes resulting from a small (here 10^{-4} a.u. = 514.2×10^{-4} V nm^{-1}) δ-function-like electric field along each axis. Then, using the Fourier transform of the dipole moment, we can construct the complex polarizability tensor, and, eventually, dipole strength function. Details can be found in ref. 60. For the calculation of hole transfer properties, we generate the initial state for RT-TDDFT using CDFT, setting the charge values to those obtained through the Löwdin analysis, apart from the oxidized atom, the charge of which is increased by +1, *i.e.*, a hole is created. Löwdin population analysis was integrated into the RT-TDDFT module of NWChem for the calculation of each fragments charge at each time step.[45] It is much less basis-set dependent and does not display extremely fast charge oscillations that Mulliken analysis (the default scheme in NWChem's RT-TDDFT implementation) artificially introduces in charge transfer simulations, thus giving a clearer picture of charge transfer. The claim that Löwdin population analysis is more appropriate for the problem at hand than Mulliken population analysis is substantiated by the form of the total dipole moment oscillations, which are similar to charge oscillations obtained by Löwdin population analysis, in the sense that they

do not show those extremely fast oscillations but have a frequency content similar to that obtained for charge osccillations by Löwdin population analysis.[36,44,45] In a Gaussian basis set, it is natural to use the single particle reduced density matrix, whose time evolution is governed by the von Neumann equation. The Magnus propagator is used in NWChem's RT-TDDFT implementation: it is stable and conserves the density matrix idempotency.[60] At the end of each time step, the charge is calculated at each atom, along with the dipole moment. After tests, we used a time step of 0.5 a.u. The atomic unit of time, $\hbar/E_H \approx 0.02418$ fs, E_H is the Hartree energy. We performed four-step calculations: (1) geometry optimization, (2) ground state DFT, (3) vibrational analysis, (4) RT-TDDFT. These four-step calculations were performed multiple times, each time at a specific level of theory. That is, each time DFT, CDFT, and RT-TDDFT calculations were carried out at the same level of theory. We employed the B3LYP functional.[63–66] We have performed checks with many different functionals in our previous works.[9,10] Screened hybrid density functionals,[67] might be useful for some applications. Given the large amount of calculations performed in the present work with many different levels of theory of DFT-related methods, the large amount of calculations performed with TB-related methods, and our comparisons with experimental results where available, an exhaustive examination of a large number of functionals exceeds the scope of this work. For all DFT-related methods, we used the following basis sets: 3-21G*,[68,69] 6-31G*,[70,71] 6-31G**,[70,71] 6-31++G**,[69,72–74] 6-311G**,[69,75] 6-311++G**,[69,75] cc-pVDZ,[76,77] cc-pVTZ,[76,77] and STO-3G.[78] Typically, we performed geometry optimization, each time at the same level of theory, and studied the vibrational modes as included in NWChem.

2.3 Influence of vibrations

The electronic and optical properties of typical insulators and semiconductors are affected by atomic motion through electron–phonon interaction: not only band gaps change with temperature, but even at absolute zero temperature, zero-point motion causes band-gap renormalization.[79] Molecular excited state calculations are systematically improved by including nuclear quantum motion.[80]

For the first members in the series of polyynes and dicyanopolyynes, we have evaluated the effect of nuclear motion absorption spectra and oxidation dynamics. The influence of nuclear motion to a quantum mechanical observable at temperature *T*, $\hat{O}(T)$, can be expressed *via* the standard quantum mechanical expectation value

$$O(T) = \frac{1}{Z}\sum_s \langle\chi_s(\vec{u})|\hat{O}(\vec{u})|\chi_s(\vec{u})\rangle e^{-\frac{E_s}{k_B T}}. \quad (25)$$

Here $\vec{u}$ is the nuclear displacement vector, $|\chi_s(\vec{u})\rangle$ is a vibrational eigenstate on the ground state potential energy surface with energy E_s, $Z = \sum_s e^{-\frac{E_s}{k_B T}}$ is the partition function, and $\hat{O}(\vec{u})$ is the observable of interest once the system is displaced by $\vec{u}$.

This journal is © the Owner Societies 2024

Phys. Chem. Chem. Phys., 2024, **26**, 22149–22163 | **22153**

Within the harmonic approximation for the ground state potential, we can substitute $|\chi_s(\vec{u})\rangle$ with the wavefunctions of the quantum harmonic oscillator, obtaining[81]

$$O(T) = \int d\vec{u} |\Phi(\vec{u}, T)|^2 O(\vec{u}). \tag{26}$$

$|\Phi(\vec{u},T)|^2$ is the harmonic density function at temperature T, given by

$$|\Phi(\vec{u}, T)|^2 = \prod_\nu \frac{\exp\left(-\dfrac{u_\nu^2}{2\sigma_\nu^2(T)}\right)}{\sqrt{2\pi}\sigma_\nu(T)}, \tag{27}$$

where

$$\sigma_\nu^2(T) = \frac{1}{2\omega_\nu}\coth\left(\frac{\omega_\nu}{2k_B T}\right). \tag{28}$$

The index ν runs over vibrational modes and ω_ν is the frequency of mode ν. Atomic units and mass-weighted coordinates have been used.

The above expressions rely on the Born–Oppenheimer approximation, which is generally acceptable for organic systems.[79] The harmonic approximation can break down in extended molecular crystals and particularly at elevated temperatures.[82,83] However, it is generally justified for molecules in vacuum and at low temperatures.[80] The approximation to molecular vibrations made above can lead to errors, when studying molecular properties at room temperature, where highly anharmonic modes can be activated. Here we focus on the effects of nuclear quantum motion on electronic observables, where vibrational modes are active with their zero-point energy, $\frac{\hbar\omega}{2}$, in a regime that anharmonicity is assumed to be negligible.

Eqn (26) can be approximated *via* the Monte Carlo method by generating a sample of configurations $\vec{u}$, according to the harmonic distribution at a specific temperature T, so that the expectation value of the observable $O(T)$ can be computed as an average of the sample values. This method relies on no adjustable parameters, apart from the choice of DFT functional and basis set, which are fixed throughout the entire series of calculations. Other methods were proposed in the past, such as the nuclear ensemble approach used within the quantum chemistry community[84,85] or methods generating initial nuclear configurations from a Boltzmann distribution to sample vibrational averages of observables,[86,87] although the latter would not capture the effects of zero-point motion. In this work, to sample the integral of eqn (26), we generate 100 displaced configurations for each molecule at $T = 0$ K and obtain the renormalized absorption spectra, as well as quantities related to hole transfer (using RT-TDDFT), *versus* those of their 'static', frozen, conformations.

3 Results

For each molecule, with DFT-related methods, using NWChem,[61] we optimize geometry, extract vibrational modes and obtain the electronic structure including population analysis. Then, we create a hole at a site by CDFT and we obtain the spatial and temporal evolution by RT-TDDFT. For each molecule, in TB, we use the optimized geometry, to obtain all TB-related quantities. After oxidation, in TB, we obtain the time-dependent probability of finding the hole at each orbital and at each atom. Then, averaging over time, we derive the corresponding mean over time probabilities. In RT-TDDFT, the excess charge as a function of time, $q_{\text{excess}}(t)$, can be calculated from the charge as a function of time $q(t)$ minus the charge at time zero (when oxidation takes place) $q(0)$ [which is the outcome of CDFT, except for the oxidized site whose charge is increased by +1], *i.e.*, as $q_{\text{excess}}(t) = q(t) - q(0)$. Another possibility would be to calculate $q_{\text{excess}}(t)$, from $q(t)$ minus the charge of the neutral atom, *i.e.*, as $q_{\text{excess}}(t) = q(t) - q_{\text{neutral atom}}$. After averaging $q_{\text{excess}}(t)$ over time, we obtain the mean excess charge, which is comparable to the TB mean probabilities. We are also interested in time-dependent total dipole moment components. From the time-dependent probabilities and dipole moment components, we analyse, *via* Fourier Transform, the frequency content of carrier movement. Finally, we calculate the mean hole transfer rates from orbital to orbital (not shown in this article, for brevity), and from atom to atom or from site to site. For example, provided that we initially place the carrier at site i, the mean transfer rate from site i to site j is defined as usual,[9,36,88] as $k_{ij} := \langle q_{\text{excess}\,j}(t)\rangle/t_{\text{mean}\,ij}$ in RT-TDDFT or $k_{ij} := \langle|C_j(t)|^2\rangle/t_{\text{mean}\,ij}$ in TB, where $t_{\text{mean}\,ij}$ is the time it takes for $q_{\text{excess}\,j}(t)$ in RT-TDDFT or $|C_j(t)|^2$ in TB to reach its mean value for the first time.

Fig. 2 shows a comparison between the optimized geometries of one example of polyynes (H$_2$C$_{10}$, *cf.* Section 3.1) and one of dicyanopolyynes (N$_2$C$_{10}$, *cf.* Section 3.2), at the B3LYP/cc-pVTZ level of theory. We have performed calculations at different levels of theory; results converge nicely as we move to larger basis sets (cc-pVTZ is the largest that we tried). For polyynes, we have alternating short and long bonds between carbon atoms with the first carbon–carbon bond being short, while carbon–hydrogen bonds are even shorter. For dicyanopolyynes we have alternating short and long bonds between carbon atoms with the first carbon–carbon bond being long, while nitrogen–carbon bonds are even shorter. In Fig. 3
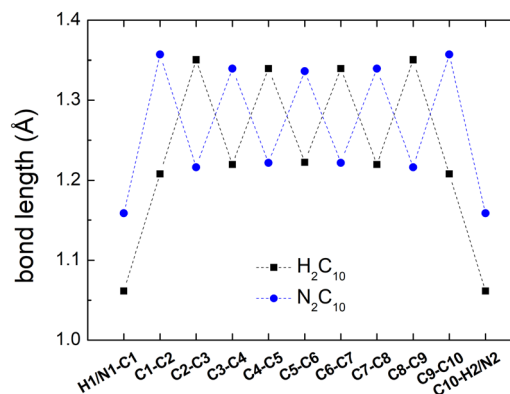

Fig. 2 Optimized geometries of one example of polyynes (C$_{10}$H$_2$) and one of dicyanopolyynes (C$_{10}$N$_2$), at the B3LYP/cc-pVTZ level of theory.

22154 | *Phys. Chem. Chem. Phys.*, 2024, **26**, 22149–22163

This journal is © the Owner Societies 2024

we compare the optimized lengths of polyynes (H_2C_{2m}) and dicyanopolyynes (N_2C_{2m}), for $m = 1, 2, \ldots, 5$, at the B3LYP/cc-pVTZ level of theory. It appears that lengths increase in a parallel linear fashion, with dicyanopolyynes being longer.

Additional data for the comparison between the ground state properties of polyynes (H_2C_{2m}) and dicyanopolyynes (N_2C_{2m}), $m = 1, 2, \ldots, 5$, at the B3LYP/cc-pVTZ level of theory, can be found in the ESI:† total DFT energies, contributions of one-electron terms, Coulomb repulsion, exchange correlation, nuclear repulsion to the total DFT energies, and HOMO–LUMO gaps.

3.1 Polyynes

We denote polyynes with alternating short and long bonds and $N_C = n$ carbon atoms by *pol-n-sl*, *e.g.*, *pol-6-sl*, of $D_{\infty h}$ symmetry, with two CH– end groups, possesses 26 valence electrons. We report results for *pol-2-sl* (H_2C_2), *pol-4-sl* (H_2C_4), *pol-6-sl* (H_2C_6), *pol-8-sl* (H_2C_8), and *pol-10-sl* (H_2C_{10}) and we focus on the median of the series, *pol-6-sl* (H_2C_6), for illustrative purposes.

The TB variant that we use recruits one s-type orbital for hydrogen, one s-type orbital and one (triplet) p-type orbital for carbon and nitrogen. The closest Gaussian basis set that we could imagine is the "minimal" STO-3G basis set that has the same number and (nominally) type of valence orbitals. In the ESI,† we present the Löwdin population analysis, at the B3LYP/STO-3G level of theory, for various *pol-n-sl* molecules with even $N_C = n$. Due to higher electronegativity, C atoms have slightly higher electron charge than neutral C atoms; the opposite holds for H atoms. As the length of the chain is increased, excess charge is distributed among more carbon atoms; less charge remains at hydrogen atoms.

Fig. 4 shows the vibrational frequencies of *pol-n-sl* molecules, with even $N_C = n$, at the B3LYP/6-31G* level of theory. Specific patterns appear: (a) two high-frequencies for all molecules, related to vibrations of hydrogen atoms. (b) Medium frequencies, whose number is increased, as the chain length is increased. These correspond to vibrations of carbon atoms along the chain. (c) Low frequencies, corresponding to vibrations that change the symmetry of the one-dimensional chain, *i.e.*, bend the rod.
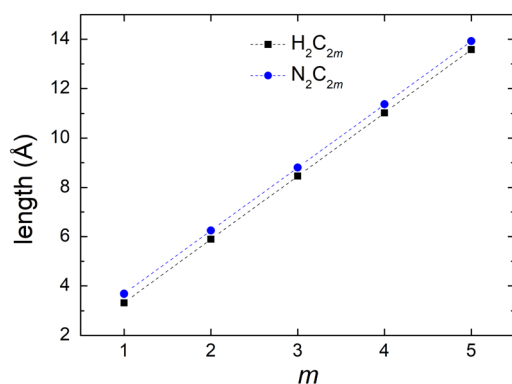

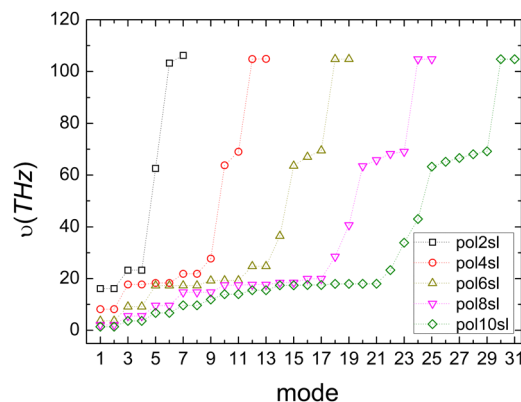**Fig. 4** Vibrational frequencies of *pol-n-sl* molecules with even $N_C = n$ ($n = 2, 4, 6, 8, 10$) at the B3LYP/6-31G* level of theory.

In Fig. 5 we compare experimental ionization and excitation energies of *pol-n-sl* polyynes with even $N_C = n$ with theoretical ones, obtained by TB with all valence orbitals, DFT and RT-TDDFT. The quantities in Fig. 5 are vertical values, *i.e.*, calculated or measured at fixed geometry. The experimental ionization energy, IE_{exp}, is taken from ref. 89. Similar values for $n = 2, 4, 6, 8$, respectively, are given in ref. 90–93. The experimental excitation energy, EE_{exp}, is obtained combining information from ref. 42, 94 and 95 (gas-phase data). In the experiment,[94] there exist two series (*i.e.*, as n changes) of peaks: series A, at lower energies is approximately two orders of magnitude weaker than series B. Similar, with series B excitation energies are given in ref. 41 and 95, *i.e.*, 8.6 eV, 6.8 eV, 6.0 eV, 4.9 eV, for $n = 4, 6, 8, 10$, respectively. *Via* TB with all valence orbitals, we obtain the molecular eigenenergies and eigenvectors and, in particular, their HOMO and LUMO energies and their HOMO–LUMO gap. If we assume that for TB the absolute value of the HOMO energy, $|E_H|$, could be considered as the ionization
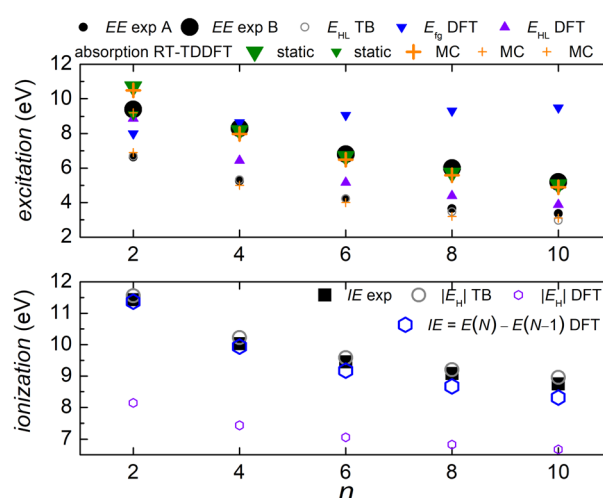

Fig. 3 Optimized lengths of polyynes (H_2C_{2m}) and dicyanopolyynes (N_2C_{2m}), $m = 1, 2, \ldots, 5$, at the B3LYP/cc-pVTZ level of theory.

Fig. 5 Excitation energy *EE* (top) and ionization energy *IE* (bottom) for polyynes. Comparison of experimental with theoretical data. The DFT and RT-TDDFT results shown were obtained at the B3LYP/cc-pVTZ level of theory.

This journal is © the Owner Societies 2024

Phys. Chem. Chem. Phys., 2024, **26**, 22149–22163 | **22155**

energy, IE, then we have an overestimation of ≈ 1–2% compared to the experiment. If we assume that for TB the HOMO–LUMO gap, E_{HL}, could be considered as the excitation energy, EE, then, for series A excitation energies we have a deviation of only 0–1% for $n = 2, 4, 6$, and underestimations of ≈ 5 and 11%, for $n = 8$ and $n = 10$, respectively, compared to the experiment. We notice that the experimental data for these weak transitions are only given in an graph in ref. 94 and we underline that taking the HOMO–LUMO gap equal to EE is a crude approximation since we ignore excitonic effects and re-arrangement of the molecule when excited. In TB, the HOMO and LUMO are typically of similar symmetry, *cf.* Fig. 6 (for all polyyne molecules, *cf.* ESI†); therefore, the HOMO–LUMO transition should be close to optically forbidden in the dipole approximation, *i.e.*, it should have negligible oscillator strength. This is why we compare the TB HOMO–LUMO gaps with series A peaks.

Let us call $E(M)$ the total energy of a system with M electrons, and $E_H(M)$, $E_L(M)$ its HOMO and LUMO eigenenergy, respectively. From DFT, we can calculate the ionization energy as $IE = E(N) - E(N-1)$. IE should be equal to $-E_H(N)$, if the molecular eigenstates remained unaffected by removal of one electron (but they are not) and if DFT could precisely estimate E_H (but it can not, *cf.* lower panel of Fig. 5). From DFT, we can also calculate the electron affinity, as $EA = E(N+1) - E(N)$. EA should be equal to $-E_L(N)$, if the molecular eigenstates remained unaffected by addition of one electron (but they are affected) and if DFT could precisely estimate E_L (but it can not). Then, we can estimate the fundamental gap as $E_{fg} = IE - EA$. E_{fg} should be $E_L - E_H := E_{HL}$, if the molecule remained unaffected by addition or removal of one electron, but it is not. We observe in the upper panel of Fig. 5 that there is a great difference between E_{fg} and E_{HL}. The values we show in Fig. 5 were obtained at the B3LYP/cc-pVTZ level of theory. This way, from DFT, for IE we have an underestimation of 3–8%. It seems that EA and hence E_{fg} are far from successful: we observe that E_{fg} is an increasing function of n, a behaviour inverse of the experimentally expected. The differences between various flavours of gaps, *e.g.* "band gap", "HOMO–LUMO gap", "fundamental gap", "optical gap", "transport gap" are explained, *e.g.*, in ref. 43.

To evaluate the optical gap, absorption spectra can be obtained by RT-TDDFT,[60] taking advantage of the procedure described at the NWCHEM website. We obtained absorption spectra in the static case, as well as using deformations and the MC sampling technique explained in Subsection 2.3. Primary peaks are denoted by large down-pointing triangles (static) and large crosses (MC) in Fig. 5, and secondary peaks are denoted by smaller versions of the respective shapes. For $n = 2$, the peaks for 9.1 eV (static) and 9.2 eV (MC) are weak, and there is another series of very weak peaks revealed only by MC, which fall onto experimental peak A series: the form of these very weak peaks revealed by the average MC configuration are for $n = 2$ a peak, for $n = 4$ a shoulder, then, for $n = 6, 8, 10$ we can only see inflection points.

Fig. 6 depicts the molecular eigenenergies of *pol-6-sl* and the character of each eigenstate, as obtained *via* TB. We already mentioned that by character we mean the analysis of molecular states into valence atomic states. In *pol-6-sl* we have 26 valence electrons. Hence, in increasing eigenenergy, the HOMO (LUMO) corresponds to the 13th (14th) eigenstate. The molecule lies along the y-axis, so $2p_y$ orbitals lie along the chain; $2p_x$ and $2p_z$ are perpendicular to the chain. The HOMO (12–13) and the LUMO (14–15) states are degenerate and of p p π character, *i.e.*, mainly composed of $2p_x$ and $2p_z$ components overlapping laterally. Not only the HOMO and LUMO, but all eigenstates 8–15, 18–19, 21–22 are of p p π character. Other molecular states have $2s$-$2p_y$ hybrid character overlapping frontally: these correspond to the strong sp sp σ type of bonds along the chain. Finally, some molecular states are of $1s$-$2s$-$2p_y$ hybrid character: these correspond to hydrogen-carbon s sp σ bonds at the chain ends. Such analysis for all *pol-n-sl* molecules is shown in the ESI.†

Regarding oxidation dynamics, for TB, the initial conditions used in this work are all possible hole placements at a valence atomic orbital of a C (or N) atom as well as various combinations of hole placements at several or all orbitals of a C (or N) atom. We also use the "TB STO-3G" initial condition: for example, at the B3LYP/STO-3G level of theory, for *pol-6-sl*, the Löwdin population analysis, *i.e.*, the shell charges ($1s$, $2s$, $2p$), for the carbon atom C_1, are approximately: (1.99, 1.06, 3.01) for the Ground State (GS), (1.99, 0.99, 2.08) for the Localized Hole State (LHS), and their difference (GS–LHS) is (0.00, 0.07, 0.93). For "TB STO-3G", we use GS–LHS to define the distribution of the placed hole at the valence atomic orbitals: the hole is distributed 7% at the $2s$ orbital and 93% at the $2p$ orbitals. The percentage of the $2p$ orbitals is equidistributed between the $2p_x$ and $2p_z$ orbitals, because the character of HOMO is π and the π-character comes from both $2p_x$ and $2p_z$ orbitals. Similar percentages hold for the rest *polnsl* molecules.

The coordinate system for *pol-n-sl* molecules is such that they lie along the y-axis. If a hole is initially created at the $2s$ orbital of C_1, it will have to travel along the y-axis. Hence, the $2s$ and $2p_y$ time-dependent probabilities of C_1 will be interconnected. The picture is similar if we initially place the hole at the $2p_y$ orbital of C_1 or at a combination of $2s$ and $2p_y$ orbitals of C_1. Including hydrogen $1s$ orbitals, we could say that an s sp σ path is active, in the sense that in similar situations only $2s$ and $2p_y$ orbitals of carbon atoms and $1s$ orbitals of hydrogen atoms will carry the hole. A relevant initial snapshot for $n = 6$ is shown in
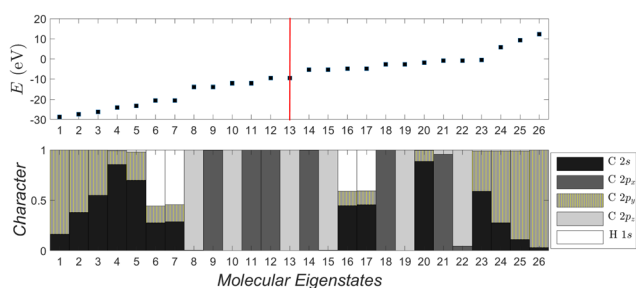

Fig. 6 Molecular eigenstates of *pol-6-sl*, as obtained *via* TB: eigenenergies and character (analysis of molecular states into atomic valence states). For a comparison of *pol-n-sl* molecules with $n = 2, 4, 6, 8, 10$, *cf.* ESI.†
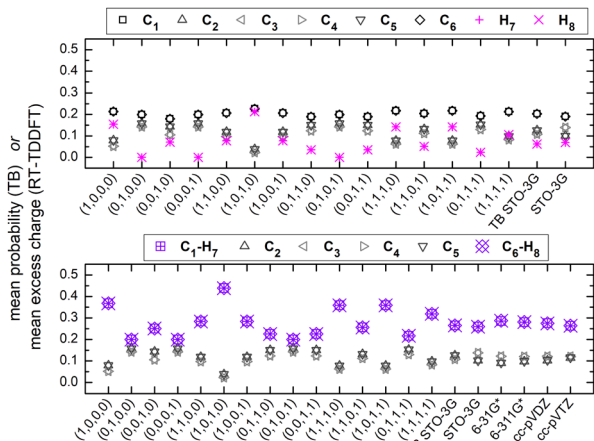
22156 | *Phys. Chem. Chem. Phys.*, 2024, **26**, 22149–22163

This journal is © the Owner Societies 2024

Fig. 7 Mean probability at each site *via* TB with various initial conditions [averaging over time the TB time-dependent probability] and mean excess charge *via* RT-TDDFT [averaging over time $q_{excess}(t) = q(t) - q(0)$] at various levels of theory, for H_2C_6. (a) Each atom corresponds to one site. (b) Each hydrogen atom forms together with its neighbouring carbon atom one site (methine). Static case. H_7 (H_8) is the hydrogen atom connected to the carbon atom C_1 (C_6).

Fig. 8 Time-dependent dipole moment of H_2C_6 obtained *via* TB with initial conditions (0,1,0,1) and TB STO-3G and *via* RT-TDDFT with basis sets STO-3G, 6-31G*, 6-311G*, cc-pVDZ, cc-pVTZ. Upper panel: using HC-sites at both ends. Lower panel: comparison with use of independent H and C sites at both ends.

Fig. 9 Frequency content of dipole moment oscillations in H_2C_6 obtained *via* FFT for TB with initial conditions (0,1,0,1), TB STO-3G and *via* RT-TDDFT with basis sets STO-3G, 6-31G*, 6-311G*, cc-pVDZ, cc-pVTZ.

the ESI,† for *pol-6-sl*. The $2p_x$ and $2p_z$ time-dependent probabilities remain zero. Alternatively, if we initially place the hole at a $2p_x$ or $2p_z$ orbital of C_1 (or at a combination of those), one (or two) p p π paths will be active.

Fig. 7 shows the mean over time probabilities at each site, for various initial conditions, with oxidation (hole creation) always at C_1 (TB) as well as the mean excess charge at various levels of theory (RT-TDDFT), for H_2C_6. These are static results. We underline that in TB, the hole is always created at C_1, while, in RT-TDDFT, the hole is either created at C_1 (upper panel) or at the first HC-site, C_1 and H_7 (lower panel). In the upper panel, each atom forms a site for RT-TDDFT at the B3LYP/STO-3G level of theory, and the hole is created at C_1. In the lower panel, in TB, the mean over time probability of each H atom is shown together with the mean over time probability of its closest C atom with which they form a methine (HC–). In RT-TDDFT the hole is created at the first methine (HC–). The RT-TDDFT results at all levels of theory are palindromic, *i.e.*, symmetrical relative to the molecular centre. This palindromicity holds also for TB, for all initial conditions. For RT-TDDFT, we depict results with $q_{excess}(t) = q(t) - q(0)$. We tried $q_{excess}(t) = q(t) - q_{neutral\ atom}$, too; then, the mean excess charges at the single carbon atoms in the middle of the chain come even closer.

Fig. 8 (top) shows the time-dependent total dipole moment in H_2C_6 with a hole, *via* RT-TDDFT and basis sets STO-3G, 6-31G*, 6-311G*, cc-pVDZ and cc-pVTZ as well as *via* TB and initial conditions (0,1,0,1) and TB STO-3G, using methine (HC–) sites at both ends. In RT-TDDFT, such fragments are defined by CDFT. In TB, we consider the fragment as located at the centre of charge of the two constituents. RT-TDDFT lines are relatively close with the exception of STO-3G; TB lines are also close. However, RT-TDDFT oscillations are faster than TB oscillations. In Fig. 8 (bottom) we observe that use of independent H and C sites at both ends instead of HC-sites hardly affects the results.
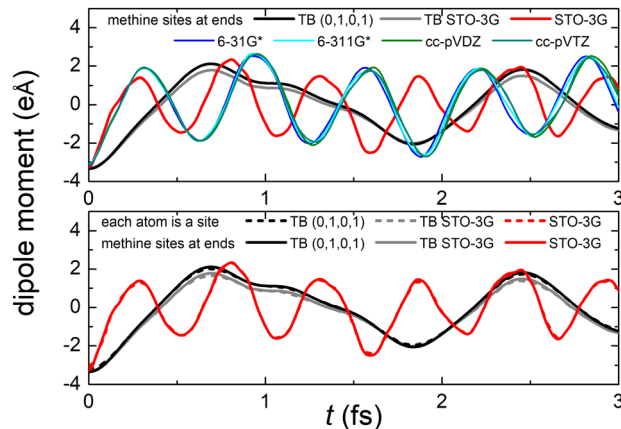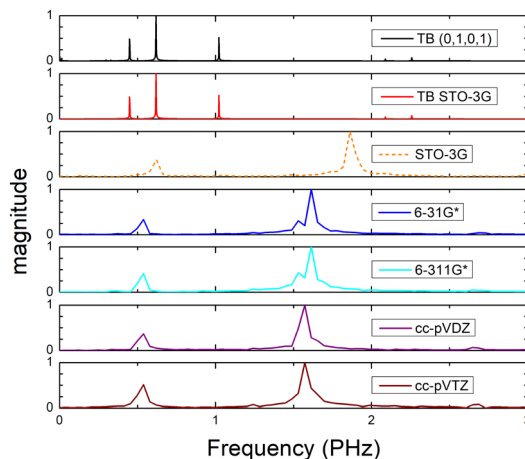
Fig. 9 shows the frequency content of total dipole moment oscillations in H_2C_6. TB curves are narrower than RT-TDDFT curves; one reason is that these RT-TDDFT curves are obtained by NWChem with time step 0.5 a.u. and time span 1000 a.u., whereas, these TB curves are obtained by custom-made matlab code with duration 500 fs ≈ 20 678.2 a.u. This time span is typically divided into 4×10^5 steps, hence the time step is 1.25×10^{-3} fs ≈ 0.05 a.u. In other words, in TB we have denser mesh and longer duration. Plainly, the TB frequency content lies clearly at lower frequencies, a deduction consistent with Fig. 8. All FFT data are for combined methine (HC–) sites at both ends.

Fig. 10 shows mean hole transfer rates, in the static case, in H_2C_6. In TB, the hole is always created at C_1. In RT-TDDFT, the hole is either created at C_1 (upper panel) or at the first HC-site, C_1 and H_7 (lower panel). In TB, transfer rates depend on the initial condition. When the hole is initially placed at a carbon 2s or $2p_y$ orbital (or at a combination of those), we observe higher
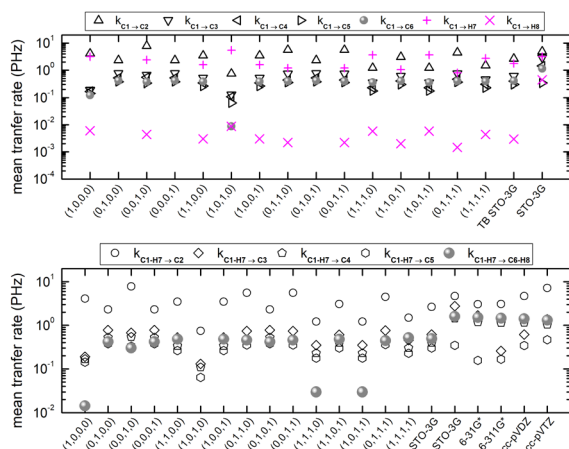
This journal is © the Owner Societies 2024

Phys. Chem. Chem. Phys., 2024, **26**, 22149–22163 | **22157**

Fig. 10 Mean hole transfer rates in H_2C_6 via TB and RT-TDDFT. Static case. H_7 (H_8) is the hydrogen atom connected to the carbon atom C_1 (C_6). Tiny values are not shown to preserve details for significant values.
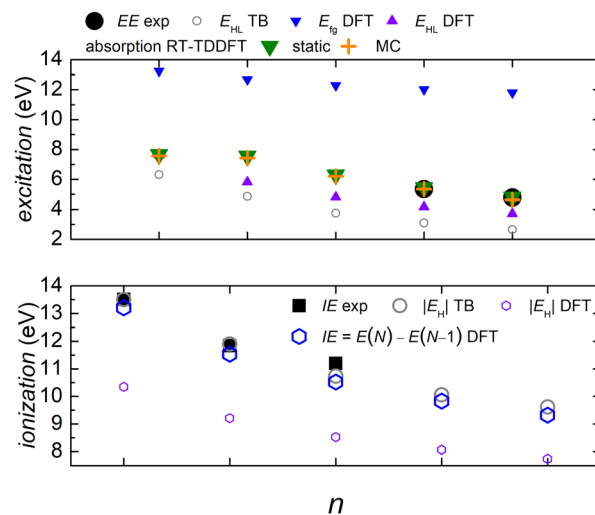

Fig. 11 Excitation energy EE (top) and ionization energy IE (bottom) for dicyanopolyynes. Comparison of experimental with theoretical data. The DFT and RT-TDDFT results shown were obtained at the B3LYP/cc-pVTZ level of theory.

transfer rates to the neighbouring hydrogen (a s sp σ path is active). When the hole is initially placed at a carbon $2p_x$ or $2p_z$ orbital (or at a combination of those), we observe negligible hole transfer rates to hydrogens (p p π paths are active).

3.2 Dicyanopolyynes (and comparison with polyynes)

We denote dicyanopolyynes with NC–, –CN end groups and n carbon atoms by N_2C_n (or dicyano-n-polyyne). They possess $D_{\infty h}$ symmetry. For example, N_2C_6 has 34 valence electrons. We report results for n = 2, 4, 6, 8, 10 and focus on the median, N_2C_6, again, for illustrative purposes.

Fig. 11 discusses EE (top) and IE (bottom) for dicyanopolyynes. The experimental ionization energy, IE_{exp}, is taken from ref. 96–99, for n = 2, 4, 6, respectively. The experimental excitation energy, EE_{exp}, for n = 8, 10 (solution), is obtained from ref. 40–42. For n = 2 (gas phase) ref. 42, citing the book,[100] gives ≈ 9.4 eV, while in ref. 101–103 for n = 2, the absorption spectrum has features ≈ in the range 238–186 nm (5.2–6.7 eV). Therefore, we are not sure about this experimental point. E_{HL} (DFT) for n = 2 is covered by absorption symbols, static and MC. We did not find other values in the literature. We speculate that the HOMO–LUMO gap cannot be seen in the absorption spectra because HOMO and LUMO have typically similar symmetry, cf. also series A in polyynes.

Fig. 12 depicts the molecular eigenenergies of dicyano-6-polyyne (N_2C_6) and the character of each eigenstate. In N_2C_6 we have 34 valence electrons. Hence, in increasing eigenenergy, the HOMO (LUMO) corresponds to the 17th (18th) eigenstate. The molecule lies along the y-axis, so $2p_y$ orbitals lie along the chain; $2p_x$ and $2p_z$ are perpendicular to the chain. The HOMO (16–17) and the LUMO (18–19) states are degenerate and of p p π character, i.e., mainly composed of $2p_x$ and $2p_z$ components overlapping laterally. Not only the HOMO and LUMO, but all eigenstates 8–11, 14–23, 26–27 are of p p π character. The other molecular states have $2s$-$2p_y$ hybrid character overlapping frontally: these correspond to the strong sp sp σ type of bonds

along the chain. Such analysis for other dicyano-n-polyynes is shown in the ESI.†

Fig. 13 shows the mean over time probabilities (TB) and the mean excess charge (RT-TDDFT), for C_6N_2. For RT-TDDFT, we depict results with $q_{excess}(t) = q(t) - q(0)$. We also tried $q_{excess}(t) = q(t) - q_{neutral\ atom}$; then, the mean excess charges at single carbon atoms in the middle of the chain come even closer. We underline that in TB, the hole is always created at N_1, while, in RT-TDDFT, the hole is either created at N_1 (upper panel) or at the first NC-site, N_1 and C_2 (lower panel). In the upper panel, each atom forms a site for RT-TDDFT, and the hole is created at N_1. In the lower panel, in TB, the mean over time probability of each N atom is shown together with the mean over time probability of its closest C atom with which they form a cyan (NC–), while in RT-TDDFT the hole is created at the first cyan (NC–). The RT-TDDFT results at all levels of theory are palindromic, i.e., symmetrical relative to the molecular centre. This palindromicity holds also for TB, for all initial conditions.

Regarding oxidation dynamics, Fig. 14 (top) shows the time-dependent total dipole moment in N_2C_6 with RT-TDDFT and basis sets STO-3G, 6-31G*, 6-311G*, cc-pVDZ and cc-pVTZ as

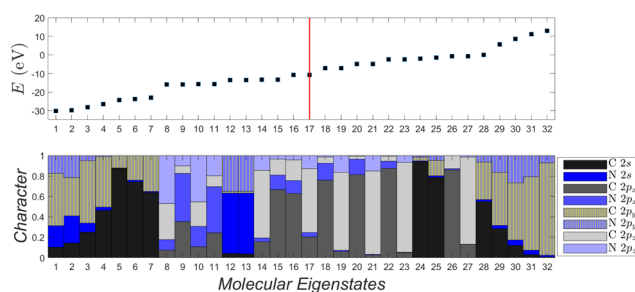**Fig. 12** Molecular eigenstates of dicyano-6-polyyne (N_2C_6): eigenenergies and character (analysis of molecular states into atomic valence states). For a comparison of dicyano-n-polyynes with n = 2, 4, 6, 8, 10, cf. ESI.†

22158 | Phys. Chem. Chem. Phys., 2024, **26**, 22149–22163

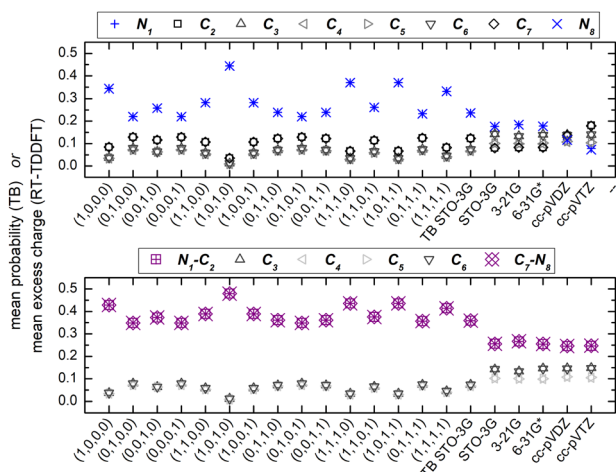This journal is © the Owner Societies 2024

Fig. 13 Mean over time probability at each site *via* TB with various initial conditions [averaging over time the TB time-dependent probability] and mean excess charge *via* RT-TDDFT [averaging over time $q_{excess}(t) = q(t) - q(0)$] at various levels of theory, for N_2C_6. (a) Each atom corresponds to one site. (b) Each nitrogen atom forms together with its neighbouring carbon atom one site (cyan).

well as with TB and initial conditions (0,1,0,1) and TB STO-3G, using cyan (NC–) sites at both ends. RT-TDDFT lines are close with a slight delay of 6-31G* and the exception of STO-3G; TB lines are not so close as in Fig. 8 (top). Again, RT-TDDFT oscillations are faster than TB oscillations. In Fig. 14 (bottom) we observe that use of independent N and C sites at both ends instead of NC-sites only slightly affects the results for TB, but has a significant effect at the minimal B3LYP/STO-3G level of theory.

Fig. 15 shows the frequency content of total dipole moment oscillations in N_2C_6. TB curves are narrower than RT-TDDFT curves; one reason is that these RT-TDDFT curves are obtained by NWChem with time step 0.5 a.u. and time span 1000 a.u., whereas, these TB curves are obtained by custom-made matlab code with duration 500 fs $\approx$ 20 678.2 a.u. This time span is
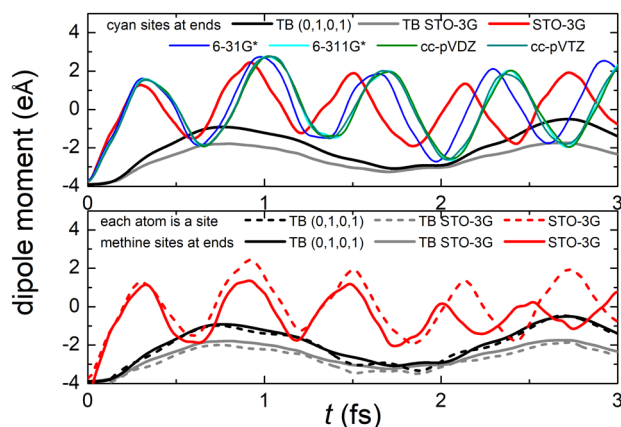
typically divided into 8×10^5 steps, hence the time step is 0.625×10^{-3} fs $\approx$ 0.025 a.u. In other words, in TB we have denser mesh and longer duration. Again, the TB frequency content is clearly at lower frequencies, a deduction consistent with Fig. 14. All FFT data are for combined cyan (NC–) sites at both ends.

Fig. 16 shows the mean hole transfer rates in N_2C_6 with TB and RT-TDDFT, in the static case. Again, generally speaking, end to end hole transfer rates predicted by RT-TDDFT are higher than those predicted by TB.

Computing carrier transfer rates in the presence of vibrations is only really meaningful if the frequency of carrier transfer is much larger than the frequency of molecular vibrations. Looking *e.g.* at Fig. 9 and 4 for polyynes, the reader can be convinced that this does appear to be the case. For such linear molecules, our calculations show that: (a) zero-point motion has almost negligible influence on the mean over time probability (TB) or mean excess charge (RT-TDDFT) to find the hole at an atom. (b) Transfer rates to middle atoms depend somehow on the basis set, probably due to orbital-based population analyses inherent weaknesses. (c) However, the transfer rate from one end of the molecule to the other end does not depend much on the basis set and it is a decreasing function of the molecular length. (d) For our linear molecules, inclusion of zero-point motion only slightly affects hole transfer rates. These findings are illustrated in Fig. 17, which shows a comparison of carrier transfer rates between the static configuration and the average over Monte Carlo samples, accounting for molecular vibrations, for polyynes as well as for dicyanopolyynes. For *polnsl* molecules, the number of short bonds is $n/2$ and the number of long bonds is $n/2 - 1$. Looking at Fig. 3 and taking the short bond length $\approx$1.2 Å and the long bond length $\approx$1.35 Å, we obtain the transfer length (ignoring the length of the C–H bonds since the hole is created at a carbon atom) as $\ell = (n/2)1.2$ Å $+ (n/2 - 1)1.35$ Å. An exponential fit of the form

Fig. 14 Time-dependent dipole moment of N_2C_6 obtained *via* TB with initial conditions (0,1,0,1) and TB STO-3G and *via* RT-TDDFT with basis sets STO-3G, 6-31G*, 6-311G*, cc-pVDZ, cc-pVTZ. Upper panel: using NC-sites at both ends. Lower panel: comparison with use of independent N and C sites at both ends instead of NC-sites.
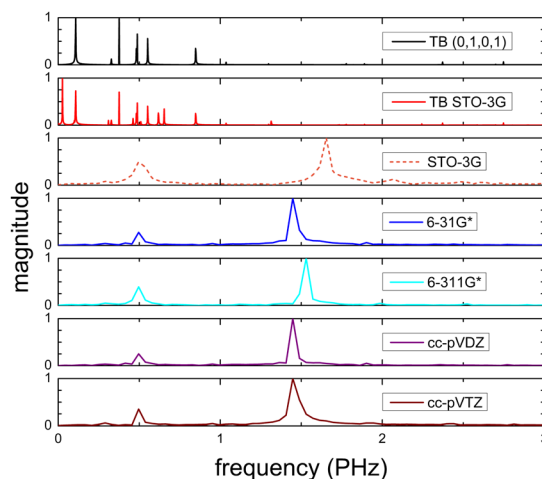

Fig. 15 Frequency content of dipole moment oscillations in N_2C_6 obtained *via* FFT for TB with initial conditions (0,1,0,1), TB STO-3G and *via* RT-TDDFT with basis sets STO-3G, 6-31G*, 6-311G*, cc-pVDZ, cc-pVTZ.

This journal is © the Owner Societies 2024

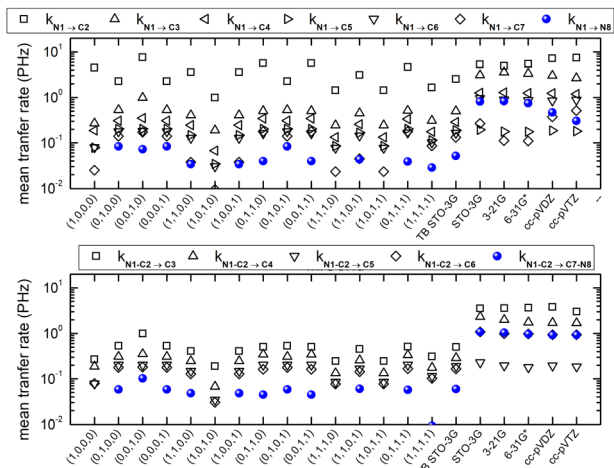*Phys. Chem. Chem. Phys.*, 2024, **26**, 22149–22163 | **22159**

Fig. 16 Mean hole transfer rates in N_2C_6 with TB and RT-TDDFT. Static case.

$k(\ell) = k_0 e^{-\beta\ell}$ gives $k_0 \approx 6.95 \pm 0.43$ PHz and $\beta \approx 0.22 \pm 0.02$ Å^{-1}, in accordance with experiments in polyene and polyyne bridges, where $\beta \approx 0.2$–0.6 Å^{-1} were obtained.[104–106] Let us now translate these transfer rates to currents, according to $I = ke$, e being the elementary charge. Then, k_0 corresponds to a current $I_0 = ek_0 \approx 1$ mA. Measuring the length in Å, $\ell = \alpha$ Å, we obtain $I \approx e^{-0.22\alpha}$ mA. That is, for 1 nm = 10 Å, we obtain $I \approx 0.11$ mA. An exponential fit (*cf.* also ref. 45) of the form $k(\ell) = k_0 e^{-\beta\ell}$ for geometrically optimized cumulenes and polyynes at the B3LYP/cc-pVTZ level of theory with $N_C = 7, \ldots, 20$, gives $\beta \approx 0.11 \pm 0.02$ Å^{-1}, whereas experimental measurements[105] give $\beta \approx 0.12 \pm 0.06$ Å^{-1}.

The influence of zero-point motion on mean over time probability (TB) or mean excess charge (RT-TDDFT) at each atom, for C_nN_2 molecules is rather small. Also, these do not depend much on the basis set. Apart from $n = 2$, the transfer ra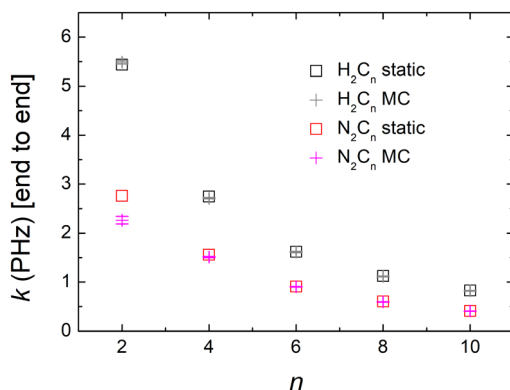te from one end (NC–) to the other end (–CN) does not depend much on the basis set. Transfer rates to middle atoms depend somehow on the basis set, probably due to orbital-based population analyses inherent weaknesses. The transfer rate from one end (NC–) to the other end (–CN) is a decreasing function of length, *cf.* Fig. 17. For C_nN_2 molecules, we have two short N–C bonds, the number of long C–C bonds is $n/2$ and the number of short C–C bonds is $n/2 - 1$. Looking at Fig. 3, and taking the N–C bond 1.17 Å, the short C–C bond length 1.2 Å and the long C–C bond length 1.35 Å, we can calculate the transfer length (including the length of the N–C bonds since the hole is created at a nitrogen atom) as $\ell = 2 \times 1.17 + (n/2) 1.35 + (n/2 - 1) 1.22$ Å. An exponential fit of the form $k(\ell) = k_0 e^{-\beta\ell}$ gives $k_0 \approx 5.80 \pm 0.29$ PHz and $\beta \approx 0.20 \pm 0.01$ Å^{-1}, for the static case, whereas for the average over Monte Carlo samples we get $k_0 \approx 4.30 \pm 0.13$ PHz and $\beta \approx 0.17 \pm 0.01$ Å^{-1}. In our linear molecules, inclusion of zero-point motion does not change transfer rates, except for a small effect in N_2C_2. We are not aware of experimental estimations of β for dicyanopolyynes.

4 Conclusion and perspectives

In this work, we employed TB- and DFT-based tools to study the electronic structure, absorption spectra, and hole transfer properties of the first members in the series of polyynes and dicyanopolyynes. Geometry optimization shows that the length of both series increases linearly, and the latter are slightly longer for the same number of carbon atoms.

The DFT-based calculation of the ionization energy as total energy difference between neutral and ionized molecule generally follows closely the available experimental results, for both series, polyynes and dicyanopolyynes. With the parametrization introduced by us, the absolute value of the HOMO energy obtained by TB follows a similar trend, close to the experimental results. The absolute value of the HOMO energy obtained by DFT follows a similar trend but far below the experimental ionization energies.

Regarding excitation energies, RT-TDDFT calculations of the absorption spectra for polyynes without the inclusion of zero-point motion are in agreement with the strong peaks found experimentally (Series B), while the inclusion of zero-point motion *via* a Monte Carlo sampling technique reveals weaker peaks at smaller energy regions, again in agreement with the weak peaks found experimentally (Series A). The latter peaks are close to the HOMO–LUMO gap predicted by TB. Agreement between RT-TDDFT-based absorption spectra and experiment occurs for dicyanopolyynes, as well (where results are available). Generally, the inclusion of zero-point motion yields small corrections to results obtained for the static (frozen) configurations in these linear molecules, contrary to cyclic ones.[9]

Furthermore, our TB method which takes into account all valence orbitals of all atoms was recruited to study the character of molecular orbitals of polyynes and dicyanopolyynes. This technique can be applied to other molecules, as well.

Our study of oxidation dynamics, by creating a localized hole at one end of the chain, reveals efficient end-to-end charge transfer for both TB and RT-TDDFT.

Fig. 17 Hole transfer rates. Comparison between the static configuration (B3LYP/cc-pVDZ level of theory) and the average over Monte Carlo samples, accounting for molecular vibrations, for polyynes and dicyanopolyynes. Standard errors are shown, but are almost invisible at this scale. (a) Black and gray symbols: end (HC–) to end (–CH) hole mean transfer rate in polyynes, *i.e.*, H_2C_n molecules. (b) Red and magenta symbols: end (NC–) to end (–CN) hole mean transfer rate in dicyanopolyynes, *i.e.*, N_2C_n molecules.

22160 | *Phys. Chem. Chem. Phys.*, 2024, **26**, 22149–22163

This journal is © the Owner Societies 2024

In this work we have studied transfer rates in short chains, *i.e.*, in oligomers. It is certainly interesting to expand to long chains. With 6 carbon atoms the polymer length is of the order of 1 nm, *cf.* Fig. 1 and 3. However, it is now possible to produce long and stable chains composed of more than 6000 carbon atoms inside double-walled carbon nanotubes.[13] Those chains have a length of the order of 1 μm. Hence, either by producing even longer chains or by combining these long chains in a matrix and allowing hopping between chains, it is possible to reach mm scales, something that would have applications in industry.

We also found that if we translate transfer rates to currents, according to $I = ke$, measuring the length in Å, $\ell = \alpha$ Å, we obtain *e.g.* in polyynes $I \approx e^{-0.22\alpha}$ mA, *i.e.*, for 1 nm = 10 Å, we obtain $I \approx 0.11$ mA. Similarly, for dicyanopolyynes. These are not negligible currents.

Furthermore, it is interesting to study charge transport, *i.e.*, study current–voltage curves and conductivity, initially in such short chains and later in long chains. Charge transport in short cumulenes and polyynes has already been studied by us in a TB model using only one orbital per site.[107] Here, we have developed a TB model that uses all valence orbitals of all atoms. Hence, is would be interesting to examine how inclusion of all valence orbitals improves our approach.

The transfer rates predicted by our TB model including all valence orbitals are lower than the ones predicted by RT-TDDFT, *cf.* Fig. 16 and 10, although much closer than the ones obtained by us in ref. 107 using the simple TB model which included only one $2p_x$ or $2p_z$ orbital per site. This is because now we allow both $2p_x\ 2p_x\ \pi$ and $2p_z\ 2p_z\ \pi$ paths as well as the $s2p_y\ s2p_y\ \sigma$ path for transfer. Maybe, we should try to include at each site orbitals higher than the valence orbitals. We will hopefully try this TB version in the future.

Author contributions

Author contributions: conceptualization, CS; methodology, CS, KL, LC; software, CS, KL, LC; validation, CS, KL, LC; formal analysis, CS, KL, LC; investigation, CS, KL, LC; resources, CS; data curation, CS, KL, LC; writing – original draft preparation, CS; writing – review and editing, CS; visualization, CS; supervision, CS; project administration, CS; funding acquisition, CS. All authors have read and agreed to the published version of the manuscript.

Data availability

Data supporting this article have been included as part of the ESI.† We also include online ESI.† NWChem is a free online software.[61] The matlab code for TB calculations will be available upon request.

Conflicts of interest

There are no conflicts to declare.

Notes and references

1 Nobel Prize in Physics, Press release. Nobel Prize Outreach, 9 October 2023, The Royal Swedish Academy of Sciences. Nobel Foundation, Stockholm, Sweden, 2023.
2 M. Ferray, A. L'Huillier, X. F. Li, L. A. Lompre, G. Mainfray and C. Manus, *J. Phys. B: At., Mol. Opt. Phys.*, 1988, **21**, L31–L35.
3 A. L'Huillier, K. J. Schafer and K. C. Kulander, *J. Phys. B: At., Mol. Opt. Phys.*, 1991, **24**, 3315–3341.
4 P. M. Paul, E. S. Toma, P. Breger, G. Mullot, F. Augé, P. Balcou, H. G. Muller and P. Agostini, *Science*, 2001, **292**, 1689–1692.
5 M. Hentschel, R. Kienberger, C. Spielmann, G. A. Reider, N. Milosevic, T. B. P. Corkum, U. Heinzmann, M. Drescher and F. Krausz, *Nature*, 2001, **414**, 509–513.
6 F. Calegari, D. Ayuso, A. Trabattoni, L. Belshaw, S. D. Camillis, S. Anumula, F. Frassetto, L. Poletto, A. Palacios, P. Decleva, J. B. Greenwood, F. Martín and M. Nisoli, *Science*, 2014, **346**, 336–339.
7 A. H. Zewail, *Angew. Chem., Int. Ed.*, 2000, **39**, 2586–2631.
8 F. Calegari and F. Martin, *Commun. Chem.*, 2023, **6**, 184.
9 K. Lambropoulos, A. M. Alvertis, A. Morphis and C. Simserides, *Phys. Chem. Chem. Phys.*, 2022, **24**, 7779–7787.
10 M. Mantela, A. Morphis, K. Lambropoulos, C. Simserides and R. Di Felice, *J. Phys. Chem. B*, 2021, **125**, 3986–4003.
11 A. S. Folorunso, F. Mauger, K. A. Hamer, D. D. Jayasinghe, I. S. Wahyutama, J. R. Ragains, R. R. Jones, L. F. DiMauro, M. B. Gaarde, K. J. Schafer and K. Lopata, *J. Phys. Chem. A*, 2023, **127**, 1894–1900.
12 W. A. Chalifoux and R. R. Tykwinski, *Nat. Chem.*, 2010, **2**, 967–971.
13 L. Shi, P. Rohringer, K. Suenaga, Y. Niimi, J. Kotakoski, J. C. Meyer, H. Peterlik, M. Wanko, S. Cahangirov, A. Rubio, Z. J. Lapin, L. Novotny, P. Ayala and T. Pichler, *Nat. Mater.*, 2016, **15**, 634–639.
14 O. Cretu, A. R. Botello-Mendez, I. Janowska, C. Pham-Huu, J.-C. Charlier and F. Banhart, *Nano Lett.*, 2013, **13**, 3487–3493.

This journal is © the Owner Societies 2024

Phys. Chem. Chem. Phys., 2024, **26**, 22149–22163 | **22161**

15 G. Wu and J. Dong, *Phys. Rev. B: Condens. Matter Mater. Phys.*, 2005, **71**, 115410.

16 X. Liu, G. Zhang and Y.-W. Zhang, *J. Phys. Chem. C*, 2015, **119**, 24156–24164.

17 M. Wang and S. Lin, *Sci. Rep.*, 2016, **5**, 18122.

18 Y. Deng and S. W. Cranford, *Comput. Mater. Sci.*, 2017, **129**, 226–230.

19 M. Tommasini, A. Milani, D. Fazzi, M. Del Zoppo, C. Castiglioni and G. Zerbi, *Phys. E*, 2008, **40**, 2570–2576.

20 A. Milani, M. Tommasini and G. Zerbi, *J. Chem. Phys.*, 2008, **128**, 064501.

21 N. R. Agarwal, A. Lucotti, D. Fazzi, M. Tommasini, C. Castiglioni, W. A. Chalifoux and R. R. Tykwinski, *J. Raman Spectrosc.*, 2013, **44**, 1398–1410.

22 A. K. Nair, S. W. Cranford and M. J. Buehler, *EPL*, 2011, **95**, 16002.

23 A. La Torre, A. Botello-Mendez, W. Baaziz, J.-C. Charlier and F. Banhart, *Nat. Commun.*, 2015, **6**, 6636.

24 M. Tommasini, D. Fazzi, A. Milani, M. Del Zoppo, C. Castiglioni and G. Zerbi, *Chem. Phys. Lett.*, 2007, **450**, 86–90.

25 A. La Magna, I. Deretzis and V. Privitera, *Eur. Phys. J. B*, 2009, **70**, 311–316.

26 P. N. D'yachkov, V. A. Zaluev, E. Y. Kocherga and N. R. Sadykov, *J. Phys. Chem. C*, 2013, **117**, 16306–16315.

27 F. Ben Romdhane, J.-J. Adjizian, J.-C. Charlier and F. Banhart, *Carbon*, 2017, **122**, 92–97.

28 A. Milani, V. Barbieri, A. Facibeni, V. Russo, A. Li Bassi, A. Lucotti, M. Tommasini, M. D. Tzirakis, F. Diederich and C. S. Casari, *Sci. Rep.*, 2019, **9**, 1648.

29 F. D. Lewis, T. Wu, Y. Zhang, R. L. Letsinger, S. R. Greenfield and M. R. Wasielewski, *Science*, 1997, **277**, 673–676.

30 C. Wan, T. Fiebig, O. Schiemann, J. K. Barton and A. H. Zewail, *Proc. Natl. Acad. Sci. U. S. A.*, 2000, **97**, 14052–14055.

31 J. Vura-Weis, M. R. Wasielewski, A. K. Thazhathveetil and F. D. Lewis, *J. Am. Chem. Soc.*, 2009, **131**, 9722–9727.

32 S. M. Mickley Conron, A. K. Thazhathveetil, M. R. Wasielewski, A. L. Burin and F. D. Lewis, *J. Am. Chem. Soc.*, 2010, **132**, 14388–14390.

33 K. Kawai and T. Majima, *Acc. Chem. Res.*, 2013, **46**, 2616–2625.

34 M. Fujitsuka and T. Majima, *Chem. Sci.*, 2017, **8**, 1752–1762.

35 T. Takada, K. Kawai, M. Fujitsuka and T. Majima, *Proc. Natl. Acad. Sci. U. S. A.*, 2004, **101**, 14002–14006.

36 C. Simserides, A. Morphis and K. Lambropoulos, *J. Phys. Chem. C*, 2020, **124**, 12834–12849.

37 M. Liu, V. I. Artyukhov, H. Lee, F. Xu and B. I. Yakobson, *ACS Nano*, 2013, **7**, 10075–10082.

38 A. Saura-Sanmartin, *Nat. Chem.*, 2024, **16**, 154–156.

39 T. Grösser and A. Hirsch, *Angew. Chem., Int. Ed. Engl.*, 1993, **32**, 1340–1342.

40 G. Schermann, T. Grösser, F. Hampel and A. Hirsch, *Chem. – Eur. J.*, 1997, **3**, 1105–1112.

41 A. Scemama, P. Chaquin, M.-C. Gazeau and Y. Bénilan, *J. Phys. Chem. A*, 2002, **106**, 3828–3837.

42 A. Scemama, P. Chaquin, M.-C. Gazeau and Y. Bénilan, *Chem. Phys. Lett.*, 2002, **361**, 520–524.

43 J.-L. Bredas, *Mater. Horiz.*, 2014, **1**, 17–19.

44 C. Simserides, A. Morphis and K. Lambropoulos, *Materials*, 2020, **13**, 3979.

45 A. Morphis, *PhD Thesis*, National and Kapodistrian University of Athens, Greece, 2023.

46 W. A. Harrison, *Electronic Structure and the Properties of Solids: the Physics of the Chemical Bond*, Dover, New York, 2nd edn, 1989.

47 W. A. Harrison, *Elementary Electronic Structure*, World Scientific, River Edge, NJ, 1999.

48 F. Banhart, *Beilstein J. Nanotechnol.*, 2015, **6**, 559–569.

49 S. Cahangirov, M. Topsakal and S. Ciraci, *Phys. Rev. B: Condens. Matter Mater. Phys.*, 2010, **82**, 195444.

50 V. I. Artyukhov, M. Liu and B. I. Yakobson, *Nano Lett.*, 2014, **8**, 4224–4229.

51 F. Cataldo, *Polyhedron*, 2004, **23**, 1889–1896.

52 S. Petrie and Y. Osamura, *J. Phys. Chem. A*, 2004, **108**, 3623–3631.

53 M. Agúndez, J. Cernicharo, P. de Vicente, N. Marcelino, E. Roueff, A. Fuente, M. Gerin, M. Guélin, C. Albo, A. Barcia, L. Barbas, R. Bolaño, F. Colomer, M. C. Diez, J. D. Gallego, J. Gómez-González, I. López-Fernández, J. A. López-Fernández, J. A. López-Pérez, I. Malo, J. M. Serna and F. Tercero, *Astron. Astrophys.*, 2015, **579**, L10.

54 M. Agúndez, N. Marcelino and J. Cernicharo, *Astrophys. J. Lett.*, 2018, **861**, L22.

55 M. Agúndez, C. Cabezas, N. Marcelino, R. Fuentetaja, B. Tercero, P. de Vicente and J. Cernicharo, *Astron. Astrophys.*, 2023, **669**, L1.

56 J. C. Slater and G. F. Koster, *Phys. Rev.*, 1954, **94**, 1498–1524.

57 P. Hohenberg and W. Kohn, *Phys. Rev.*, 1964, **136**, B864.

58 W. Kohn and L. J. Sham, *Phys. Rev.*, 1965, **140**, A1133.

59 E. Runge and E. K. U. Gross, *Phys. Rev. Lett.*, 1984, **52**, 997.

60 K. Lopata and N. Govind, *J. Chem. Theory Comput.*, 2011, **7**, 1344.

61 E. Aprà, E. J. Bylaska, W. A. de Jong, N. Govind, K. Kowalski, T. P. Straatsma, M. Valiev, H. J. J. van Dam, Y. Alexeev, J. Anchell, V. Anisimov, F. W. Aquino, R. Atta-Fynn, J. Autschbach, N. P. Bauman, J. C. Becca, D. E. Bernholdt, K. Bhaskaran-Nair, S. Bogatko, P. Borowski, J. Boschen, J. Brabec, A. Bruner, E. Cauët, Y. Chen, G. N. Chuev, C. J. Cramer, J. Daily, M. J. O. Deegan, T. H. Dunning Jr., M. Dupuis, K. G. Dyall, G. I. Fann, S. A. Fischer, A. Fonari, H. Früchtl, L. Gagliardi, J. Garza, N. Gawande, S. Ghosh, K. Glaesemann, A. W. Götz, J. Hammond, V. Helms, E. D. Hermes, K. Hirao, S. Hirata, M. Jacquelin, L. Jensen, B. G. Johnson, H. Jónsson, R. A. Kendall, M. Klemm, R. Kobayashi, V. Konkov, S. Krishnamoorthy, M. Krishnan, Z. Lin, R. D. Lins, R. J. Littlefield,

22162 | *Phys. Chem. Chem. Phys.*, 2024, **26**, 22149–22163

This journal is © the Owner Societies 2024

A. J. Logsdail, K. Lopata, W. Ma, A. V. Marenich, J. Martin del Campo, D. Mejia-Rodriguez, J. E. Moore, J. M. Mullin, T. Nakajima, D. R. Nascimento, J. A. Nichols, P. J. Nichols, J. Nieplocha, A. Otero-de-la Roza, B. Palmer, A. Panyala, T. Pirojsirikul, B. Peng, R. Peverati, J. Pittner, L. Pollack, R. M. Richard, P. Sadayappan, G. C. Schatz, W. A. Shelton, D. W. Silverstein, D. M. A. Smith, T. A. Soares, D. Song, M. Swart, H. L. Taylor, G. S. Thomas, V. Tipparaju, D. G. Truhlar, K. Tsemekhman, T. Van Voorhis, A. Vázquez-Mayagoitia, P. Verma, O. Villa, A. Vishnu, K. D. Vogiatzis, D. Wang, J. H. Weare, M. J. Williamson, T. L. Windus, K. Woliński, A. T. Wong, Q. Wu, C. Yang, Q. Yu, M. Zacharias, Z. Zhang, Y. Zhao and R. J. Harrison, *J. Chem. Phys.*, 2020, **152**, 184102.

62 P. Löwdin, *J. Chem. Phys.*, 1950, **18**, 365–375.

63 A. Becke, *J. Chem. Phys.*, 1993, **98**, 5648–5652.

64 C. Lee, W. Yang and R. G. Parr, *Phys. Rev. B: Condens. Matter Mater. Phys.*, 1988, **37**, 785–789.

65 S. H. Vosko, L. Wilk and M. Nusair, *Can. J. Phys.*, 1980, **58**, 1200–1211.

66 P. J. Stephens, F. J. Devlin, C. F. Chabalowski and M. J. Frisch, *J. Phys. Chem.*, 1994, **98**, 11623–11627.

67 M. Mohammadzaheri, S. Jamehbozorgi, M. D. Ganji, M. Rezvani and Z. Javanshir, *Phys. Chem. Chem. Phys.*, 2023, **25**, 21492–21508.

68 J. S. Binkley, J. A. Pople and W. J. Hehre, *J. Am. Chem. Soc.*, 1980, **102**, 939–947.

69 T. Clark, J. Chandrasekhar, G. W. Spitznagel and P. Von Ragué Schleyer, *J. Comput. Chem.*, 1983, **4**, 294–301.

70 W. J. Hehre, R. Ditchfield and J. A. Pople, *J. Chem. Phys.*, 1972, **56**, 2257–2261.

71 P. C. Hariharan and J. A. Pople, *Theor. Chim. Acta*, 1973, **28**, 213–222.

72 W. J. Hehre, R. Ditchfield and J. A. Pople, *J. Chem. Phys.*, 1972, **56**, 2257–2261.

73 P. C. Hariharan and J. A. Pople, *Theor. Chim. Acta*, 1973, **28**, 213–222.

74 R. Ditchfield, W. J. Hehre and J. A. Pople, *J. Chem. Phys.*, 1971, **54**, 724–728.

75 R. Krishnan, J. S. Binkley, R. Seeger and J. A. Pople, *J. Chem. Phys.*, 1980, **72**, 650–654.

76 T. H. Dunning, *J. Chem. Phys.*, 1989, **90**, 1007–1023.

77 R. A. Kendall, T. H. Dunning and R. J. Harrison, *J. Chem. Phys.*, 1992, **96**, 6796–6806.

78 W. J. Hehre, R. F. Stewart and J. A. Pople, *J. Chem. Phys.*, 1969, **51**, 2657–2664.

79 A. Miglio, V. Brousseau-Couture, E. Godbout, G. Antonius, Y.-H. Chan, S. G. Louie, C. Michel, M. Giantomassi and X. Gonze, *npj Comput. Mater.*, 2020, **6**, 167.

80 T. J. H. Hele, B. Monserrat and A. M. Alvertis, *J. Chem. Phys.*, 2021, **154**, 244109.

81 B. Monserrat, *J. Phys.: Condens. Matter*, 2018, **30**, 083001.

82 A. M. Alvertis and E. A. Engel, *Phys. Rev. B*, 2022, **105**, L180301.

83 A. M. Alvertis, J. B. Haber, E. A. Engel, S. Sharifzadeh and J. B. Neaton, *Phys. Rev. Lett.*, 2023, **130**, 086401.

84 R. Crespo-Otero and M. Barbatti, *Theor. Chem. Acc.*, 2012, **131**, 1–14.

85 S. Bai, R. Mansour, L. Stojanović, J. M. Toldo and M. Barbatti, *J. Mol. Model.*, 2020, **26**, 107.

86 W. L. Hase, R. J. Duchovic, X. Hu, A. Komornicki, K. F. Lim, D.-H. Lu, G. H. Peslherbe, K. N. Swamy, S. V. Linde, A. Varandas and R. J. Wolf, *QCPE*, 1996, **16**, 671.

87 G. H. Peslherbe, H. Wang and W. L. Hase, in *Monte Carlo Methods in Chemical Physics*, ed. I. Prigogine and S. A. Rice, John Wiley & Sons, Ltd, 1999, ch. Monte Carlo Sampling for Classical Trajectory Simulations, vol. 105, pp. 171–201.

88 C. Simserides, *Chem. Phys.*, 2014, **440**, 31–41.

89 R. I. Kaiser, B. J. Sun, H. M. Lin, A. H. H. Chang, A. M. Mebel, O. Kostko and M. Ahmed, *Astrophys. J.*, 2010, **719**, 1884.

90 P. Plessis and P. Marmet, *Int. J. Mass Spectrom. Ion Processes*, 1986, **70**, 23–44.

91 G. Bieri, A. Schmelzer, L. Åsbrink and M. Jonsson, *Chem. Phys.*, 1980, **49**, 213–224.

92 G. Bieri, F. Burger, E. Heilbronner and J. P. Maier, *Helv. Chim. Acta*, 1977, **60**, 2213–2233.

93 M. Allan, E. Heilbronner, E. Kloster-Jensen and J. Maier, *Chem. Phys. Lett.*, 1976, **41**, 228–230.

94 R. Gleiter and G. Haberhauer, *Aromaticity and Other Conjugation Effects*, Wiley-VCH, 1st edn, 2012.

95 E. Kloster-Jensen, H.-J. Haink and H. Christen, *Helv. Chim. Acta*, 1974, **57**, 1731–1744.

96 L. Åsbrink, W. von Niessen and G. Bieri, *J. Electron Spectrosc. Relat. Phenom.*, 1980, **21**, 93–101.

97 G. Bieri, E. Heilbronner, V. Hornung, E. Kloster-Jensen, J. P. Maier, F. Thommen and W. von Niessen, *Chem. Phys.*, 1979, **36**, 1–14.

98 S. Leach, M. Schwell, G. A. Garcia, Y. Benilan, N. Fray, M.-C. Gazeau, F. Gaie-Levrel, N. Champion and J.-C. Guillemin, *J. Chem. Phys.*, 2013, **139**, 184304.

99 R. E. Connors, J. L. Roebber and K. Weiss, *J. Chem. Phys.*, 1974, **60**, 5011–5024.

100 G. Herzberg, *Molecular spectra and molecular structure*, D. van Nostrand, 1945.

101 R. B. Mooney and H. G. Reid, *Nature*, 1931, **128**, 271–272.

102 R. B. Mooney and H. G. Reid, *Proc. R. Soc. Edinburgh*, 1933, **52**, 152–158.

103 S.-C. Woo and R. M. Badger, *Phys. Rev.*, 1932, **39**, 932–937.

104 J. M. Tour, *Chem. Rev.*, 1996, **96**, 537–554.

105 V. Grosshenny, A. Harriman and R. Ziessel, *Angew. Chem., Int. Ed. Engl.*, 1996, **34**, 2705–2708.

106 S. B. Sachs, S. P. Dudek, R. P. Hsung, L. R. Sita, J. F. Smalley, M. D. Newton, S. W. Feldberg and C. E. D. Chidsey, *J. Am. Chem. Soc.*, 1997, **119**, 10563–10564.

107 K. Lambropoulos and C. Simserides, *Phys. Chem. Chem. Phys.*, 2017, **19**, 26890–26897.

This journal is © the Owner Societies 2024

Phys. Chem. Chem. Phys., 2024, **26**, 22149–22163 | **22163**